Low-dimensional representations and anisotropy of model rotor versus porous disk wind turbine arrays

Elizabeth H. Camp and Raúl Bayoán Cal

Phys. Rev. Fluids **4**, 024610 — Published 27 February 2019

DOI: 10.1103/PhysRevFluids.4.024610

Low dimensional representations and anisotropy of model rotor versus porous disk wind turbine arrays

Elizabeth H. Camp* and Raúl Bayoán Cal†

Portland State University, Department of Mechanical and Materials Engineering

(Dated: January 21, 2019)

Abstract

An experimental study of the wake of a model horizontal axis wind turbine with a three-bladed rotor and a turbine with a stationary disk is done within a wind turbine array in order to compare the structure of these wakes. Measurements of the flow field surrounding the center turbine in the fourth row of a 4×3 array are made with stereo particle image velocimetry. Rotational effects of the blade are evident in the cross-stream mean velocity component in the rotor case and are absent in the disk case. The second and third invariants of the Reynolds stress anisotropy tensor have larger ranges in the wake of the rotor case than in the disk case with the disk case displaying higher levels of anisotropy trailing the top tip, a key location relating to kinetic energy entrainment. Application of the proper orthogonal decomposition indicates a greater emphasis on intermediate scales in the near wake of the rotor case in comparison to the disk case with such differences being mitigated in the far wake. The eigenfunction of the lowest rank mode, which contains the highest turbulence kinetic energy, displays coherence in both the near and far wake in the rotor case while the disk wake lacks such apparent organization. Based on the discrepancies in the structure and scales of the wake of the rotor versus that of the disk, careful judgment is advised in order to apply stationary disk parameterizations in modeling applications.

* betsy.h.camp@gmail.com

† rcal@pdx.edu

I. INTRODUCTION

The worldwide installed wind energy capacity nearly doubled between 2012 and 2016 with a growth of 13% between 2015 and 2016 alone [1]. Continued growth in the wind energy sector is projected to be 11-15% annually through 2020 assuming no major changes in global policy. With the increase in implementation of wind energy technology comes the need to increase the available information and the understanding of the salient phenomena involved. Wind turbine wakes are a key issue in wind farms since most turbines, excluding those at the periphery of the farm, are impacted by the wakes of upstream turbines.

Since the wake of upstream turbines influence subsequent turbines, the properties of turbine wakes are an important factor in the function of wind turbine arrays from a variety of perspectives. For example, power generation in turbine arrays has been shown to be greatly altered by the presence of upstream turbine wakes [2]. Additionally, farm layout optimization is not only related to local wind resources and terrain but is heavily influenced by the existence and persistence of wakes from upstream turbines [3]. Furthermore, structural loads on downstream turbines are modified by the presence of wakes from upstream turbines [4, 5] not only due to changes in turbulence intensity but also owing to changes in the structure of the turbulence itself [6].

Not only have computational simulations provided insights into the physics of wind turbine wakes, they are an attractive means to approach parametric studies such as optimization problems. In order to benchmark computational codes, Krogstad *et al.* compared results for seven different computational codes against wind tunnel measurements for a three-bladed scaled turbine [7]. Krogstad *et al.* reported differences in the streamwise velocity of less than 40% while discrepancies up to about 1.5 orders of magnitude were observed in the turbulence kinetic energy between the measured and LES results. A comparison between wind tunnel measurements for an actuator disc model, a two-bladed turbine model, and four LES codes was reported by Lignarolo *et al.* [8]. Streamwise velocity profiles were found by Lignarolo *et al.* to be comparable for all cases for radial locations of greater than 0.2 rotor diameters from the model hub meanwhile simulations tended to underestimate turbulence intensity trailing the blade tip.

In computational studies, a model of the turbine rotor is required with the actuator disk (AD) and actuator line (AL) being two such models utilized in Large Eddy Simulations

(LES) [9]. Although creating equivalent simulations and experimental measurements has been a challenge in the wind energy community [7], computational results found using several different rotor parameterizations have been compared to experimental results in order to compare the wake behavior between these cases. Wu and Porté-Agel [10] compared two simulations using AD rotor parameterizations with a wind tunnel measurements performed on a model turbine for downstream distances up to 20 rotor diameters (D). Although the streamwise velocity was comparable for the three cases by $10D$ downstream, disparities between the cases remained in the Reynolds stresses and turbulence intensity at all downstream distances measured. Martínez-Tossas *et al.* [11] compared an AD and AL with wind tunnel measurements all with uniform inflow. Although only minor differences between the AD and AL models were present in the far wake, the AL model generated near wake flow structures at the blade root and tip that the AD model was unable to produce. For a variety of model parameters, the mean streamwise velocity found via the AD and AL were in agreement although both were significantly different from the wind tunnel measurements.

Experimental approaches have been employed to assess the efficacy of using a stationary model to represent a rotor wherein comparisons have been made between a rotor and a matched porous disk. Aubrun *et al.* [12] performed hotwire anemometry on a three-bladed rotor and a matched porous disk using two wind tunnel inflow conditions. The differences between the rotor and disk were more evident in quantities that depend on higher order moments than in the mean velocities. In quantities as sensitive as the skewness, discrepancies between the rotor and disk were not significant by three rotor diameters downstream in one inflow case. A wind tunnel experiment done by Lignarolo *et al.* [13] utilized particle image velocimetry measurements to compare the wake of a two-bladed rotor to a porous disk using a uniform inflow. For these measurements, performed downstream between $0.1D$ to $2.2D$, discrepancies in the axial velocity and turbulence intensity were not significant by $2.2D$. Discrepancies in the mean kinetic energy transport were the most significant and persisted to the furthest downstream distance measured. In a wind tunnel experiment by Camp and Cal [14], PIV measurements were taken within a $4{\times}3$ array with measurements surrounding the fourth row of turbines. The cross-stream velocity component was found to be insignificant by $3.2D$ downstream. Conditional averages of the largest magnitude term relevant to mean kinetic energy transport indicated that the mechanism of vertical mean kinetic energy entrainment in the near wake were not the same in the rotor and disk cases.

These conditional averages of the rotor and disk case were comparable in far wake.

The proper orthogonal decomposition (POD) is a well established technique used to analyze the flow structure of turbulent flows and which sorts such structures based on their energetic importance [15, 16]. The method was introduced to the fluid mechanics community by Lumley [17] and Sirovich later put forth the Snapshot POD which is better suited to spatially dense but temporally sparse data [18]. The POD, in comparison to other types of modal decompositions, is able to represent the maximum turbulence kinetic energy (TKE) using the least number of modes and it is thus optimal in the least squares sense. Since the POD orders modes based on energetic content, organized motions that represent little energy and may not be significant in the statistical sense but may be of dynamic importance may be confined to high rank modes.

While POD has been applied to analyze a large variety of turbulent flows, it has been employed on several occasions in the context of wind energy. Andersen simulated an infinitely long column of turbines and employed POD to analyze a slice of the velocity field parallel to the plane of the rotor [19]. The extracted planar velocity field illustrated the meandering of the wake shed from upstream turbines. The spatial organization of the streamwise velocity component of low rank POD modes displayed the rotational symmetry typical of axisymmetric flows. Using the same simulation, Andersen *et al.* later used POD as the basis of a reduced order model of this infinite turbine column [20]. By explicitly modeling 24 turbines with an actuator disc and using periodic boundary conditions, VerHulst and Meneveau [21] simulated a very large turbine array immersed in an atmospheric boundary layer. Counter-rotating vortex pairs in the air aloft of the array accounted for the bulk of the turbulence kinetic energy and were responsible for more than 14% of the mean kinetic energy entrained.

A simulation of a single wind turbine in the atmospheric boundary layer was reported by Bastine *et al.* [22]. Spatial modes were found to be roughly rotationally symmetric despite the presence of the atmospheric boundary layer in the simulation. Furthermore, the velocity field, energy flux, and torque were reconstructed and the most appropriate number of modes to employ in reconstructions varied depending on the quantity being reconstructed. Hamilton *et al.* performed wind tunnel measurements on aligned and staggered wind turbine arrays finding that about 1% of the total modes, which corresponds to about or about 20 modes, were needed to adequately reconstruct TKE production and flux of TKE. In addition, the residual between the reconstructed flow field and measured flow field was found to be spatially dependent. Hamilton *et al.* performed two iterations of POD on a wake of a turbine within a fully developed wind turbine boundary layer in order to describe the sub-modal organization and arrived at a correction procedure for a low order reconstruction of the Reynolds stress tensor [23]. Andersen *et al.* used an actuator line method to simulate a very large wind farm and applied POD in order to determine the length scales relevant to mean kinetic energy entrainment [24]. At the top tip of the turbine, the largest length scales relevant to mean kinetic energy entrainment were found to be on the order of the turbine spacing.

The Reynolds stress anisotropy tensor has been used as a key part of computational models. The Rotta model prescribes a linear return to isotropy [25] and forms the basis of second order models in which the return-to-isotropy term mediates the exchange of turbulence kinetic energy [26, 27]. Invariants of the Reynolds stress anisotropy tensor have been used explicitly in some subgrid scale models [28] in LES. In recent tuning-free LES models, a correlation has been observed between model coefficient and the presence of anisotropy [10]. The Reynolds stress anisotropy tensor and its invariants remain a important part of contemporary Reynolds stress and engineering models [29–31].

In addition to its uses in computational work, the Reynolds stress anisotropy tensor has been used as a means to provide a detailed characterization of turbulent flow fields in diverse applications. Such applications include rough wall boundary layers [32, 33], geophysical flows [34], drag reduction via polymer additives [35], pipe flow [36], stratified mixing layers [37] and flow influenced by wall section [38]. Using an explicit algebraic model, Gomez-Elvira *et al.* studied the anisotropy, turbulence intensity, and Reynolds stresses in the near wake of a wind turbine [39]. The degree of anisotropy was found to reach a maximum in the shear layer of the wake and the flow became more isotropic with increased downstream distance [39]. The near wake of a model horizontal axis tidal turbine was experimentally studied by Tedds *et al.* [40]. A high degree of anisotropy throughout the tidal turbine wake was found at downstream distances of $1D$ and $2D$ and a decay in the magnitude of the anisotropy was observed with increasing downstream distance. Hamilton *et al.* performed wind tunnel measurements on wind turbine arrays and characterized the anisotropy in the wakes of co-rotating versus counter rotating turbines [41]. The maximum magnitude of anisotropy found in all cases was in the near wake at wall-normal heights corresponding to the rotor top tip.

Regions of the wake associated with a high degree of mean kinetic energy flux also had elevated anisotropy.

Although important insight has been gained on the characteristics of wind turbine wakes, it is an open question as to what structural similarities and differences there may be between the wakes produced by a rotor and a stationary porous disk deep within a turbine array. In the present analysis, the Snapshot Proper Orthogonal Decomposition is used to compare the self-organized structure of the wake produced by both turbine models and the distribution of energy amongst the resulting POD modes. Furthermore, the invariants of the Reynolds stress anisotropy tensor are used to compare the anisotropic character of the two cases. The velocity fields in the near wake and far wake are reconstructed using a varying number of POD modes and the invariants of the Reynolds stress anisotropy tensor of this series of reconstructed velocity fields are computed.

II. THEORY

In the development that follows, velocities are denoted by capital letters and indicate ensemble means. Mean centered fluctuations are represented with lower case letters with a prime symbol. Overbars are used to show time averaging ($\overline{\cdots}$) while angle brackets ($\langle \cdots \rangle$) show spatial averages. The present analysis utilizes snapshot proper orthogonal decomposition (POD) as formulated by Sirovich [18] wherein bold variables represent vectorial quantities. In order to perform the Snapshot POD of the fluctuating velocity $\boldsymbol{u'}(\boldsymbol{x}, t)$, it is assumed that the fluctuating velocity can be approximated as a series of the form

$$\boldsymbol{u'}(\boldsymbol{x}, t) = \sum_{n=1}^{N} a_n(t) \boldsymbol{\phi}^{(n)}(\boldsymbol{x}), \tag{1}$$

where $a_n(t)$ is the time-dependent POD coefficient for mode n, $\boldsymbol{\phi}^{(n)}\boldsymbol{(x)}$ is the spatial POD mode for mode n, and N is the number of snapshots. The fluctuating velocity measured over P spatial positions instantaneously and which is measured at N times is arranged into the matrix $\mathring{\boldsymbol{U}}$ as

$$\mathring{\boldsymbol{U}} = \frac{1}{N} \begin{bmatrix} u_1'^1 & u_1'^2 & \cdots & u_1'^N \\ \vdots & \vdots & \ddots & \vdots \\ u_P'^1 & u_P'^2 & \cdots & u_P'^N \end{bmatrix}. \tag{2}$$

The autocovariance matrix, $\boldsymbol{C}$, can then expressed from the product $\mathring{\boldsymbol{U}}$ and its transpose as $\boldsymbol{C} = \mathring{\boldsymbol{U}}^T\mathring{\boldsymbol{U}}$. An eigenvalue problem involving $\boldsymbol{C}$ can be written as

$$\boldsymbol{C}\boldsymbol{A}_n = \lambda_n \boldsymbol{A}_n, \tag{3}$$

where $\boldsymbol{A}_n$ is the eigenvector corresponding to the eigenvalue λ_n. Physically, the eigenvalues of the POD modes describe the turbulence kinetic energy represented by their respective modes. The eigenvalues of all N modes are ordered in magnitude such that

$$\lambda_1 > \lambda_2 > \cdots > \lambda_N, \tag{4}$$

where λ_N is set to 0 during computation following Meyer *et. al* [42]. From the results of the eigenvalue problem, the normalized POD modes can then be computed by projecting the snapshot basis into the eigenvalue space then normalizing which can be expressed as

$$\boldsymbol{\phi}^{(n)} = \frac{\mathring{\boldsymbol{U}}\boldsymbol{A}_n}{||\mathring{\boldsymbol{U}}\boldsymbol{A}_n||}, \tag{5}$$

where $||\cdots||$ denotes the L_2-norm. Note that the set of eigenfunctions obtained herein are orthogonal in time rather than space. After concatenating the POD modes to form $\boldsymbol{\Psi} = \begin{bmatrix}\boldsymbol{\phi}^{(1)} & \boldsymbol{\phi}^{(2)} & \cdots & \boldsymbol{\phi}^{(N)}\end{bmatrix}$, the POD coefficients can then be found by

$$\boldsymbol{a_n} = \boldsymbol{\Psi}^{-1}\boldsymbol{u'_n}, \tag{6}$$

where the computation was carried out as matrix left division which involves QR factorization.

The time-averaged Reynolds stress tensor can be expressed in Cartesian coordinates from the fluctuations in the streamwise, wall normal, and spanwise directions denoted as u', v', w', respectively. This symmetric tensor is then represented as

$$\overline{u'_i u'_j} = \begin{bmatrix} \overline{u'u'} & \overline{u'v'} & \overline{u'w'} \\ \overline{u'v'} & \overline{v'v'} & \overline{v'w'} \\ \overline{u'w'} & \overline{v'w'} & \overline{w'w'} \end{bmatrix}. \tag{7}$$

Low-dimensional approximations of the time-averaged Reynolds stresses can be reconstructed by using a subset, S, of the POD modes by

$$\overline{(u_i'u_j')_S} = \frac{1}{M}\sum_{n=1}^{S}\sum_{m=1}^{M}(a_n(t_m))^2\phi_i^{(n)}\phi_j^{(n)}, \tag{8}$$

where the summation over all times, $t_m = 1, \ldots, M$ and subsequent multiplication by $1/M$ creates the time average. Modes are denoted are denoted as $\phi_i^{(n)}$ or $\phi_j^{(n)}$ where i or j indicates the velocity component and the n describes the mode number. Alternatively, Reynolds stresses can be reconstructed from the POD modes using a subset, S, of the POD modes directly from the eigenvalues and modes by

$$\overline{(u_i'u_j')_S} = \sum_{n=1}^{S}\lambda_n\phi_i^{(n)}\phi_j^{(n)}. \tag{9}$$

A key quantity that is related physically to the modes of the POD is the turbulence kinetic energy, k, where k is defined by the summation of the Reynolds normal stresses $\overline{u_i'u_i'}$ as

$$k = \frac{1}{2}\left(\overline{u'u'} + \overline{v'v'} + \overline{w'w'}\right). \tag{10}$$

The POD is optimal in the least-squares sense such that for a given partial sum using a subset of modes S, the turbulence kinetic energy (TKE) is maximal. The eigenvalues found by performing POD over a spatial domain Ω are related to the turbulence kinetic energy integrated over the same spatial domain and can be expressed as

$$\langle k\rangle_\Omega = \frac{1}{\Omega}\int_\Omega \frac{1}{2}\overline{u_i'u_i'}\,d\boldsymbol{x} = \sum_{n=1}^{N}\lambda_n \tag{11}$$

where $\langle k\rangle_\Omega$ is the spatially averaged turbulence kinetic energy, Ω is the spatial measurement domain, u_i' is the fluctuation in the i^{th} direction and, recalling that repeated indices imply summation, $(1/2)\overline{u_i'u_i'}$ is the definition of k.

The anisotropy of the Reynolds stress tensor can be characterized via several approaches, some of which are dependent on coordinate system. Following Lumley [43], a coordinate system independent description can be found utilizing the invariants of the Reynolds stress anisotropy tensor. Further, the normalized Reynolds stress anisotropy tensor can be written as

$$b_{ij} = \begin{bmatrix} \frac{\overline{u'u'}}{k} - \frac{1}{3} & \frac{\overline{u'v'}}{k} & \frac{\overline{u'w'}}{k} \\ \frac{\overline{u'v'}}{k} & \frac{\overline{v'v'}}{k} - \frac{1}{3} & \frac{\overline{v'w'}}{k} \\ \frac{\overline{u'w'}}{k} & \frac{\overline{v'w'}}{k} & \frac{\overline{w'w'}}{k} - \frac{1}{3} \end{bmatrix} = \frac{\overline{u_i'u_j'}}{k} - \frac{1}{3}\delta_{ij}, \tag{12}$$

where δ_{ij} is the Kronecker delta.

The second and third invariants of b_{ij} have been used to characterize the anisotropy of the turbulence [27, 43]. The second invariant, η, reflects the degree of anisotropy of the turbulence and is expressed as

$$6\eta^2 = b_{ij}b_{ji}. \tag{13}$$

The third tensor invariant, ξ, describes the shape of a characteristic spheroid and represents the balance of stresses in the stress tensor. The third invariant is described by

$$6\xi^3 = b_{ij}b_{jk}b_{ki}. \tag{14}$$

Both η and ξ are bounded and prescribe all of the states of realizable turbulence. The invariants can be displayed utilizing the anisotropic invariant map (AIM) or Lumley triangle shown in Fig. 1. The AIM shows the bounds of the invariants as well as descriptions of the extreme cases and their corresponding spheroid shapes.

The second and third invariants can be combined into a composite value referred to as the anisotropy factor, F. The anisotropy factor is computed via

$$F = 1 - 27\eta^2 + 54\xi^3. \tag{15}$$

Note that F is unity in a three-dimensional isotropic turbulence field and becomes null in cases of two dimensional turbulence.

III. EXPERIMENTAL SETUP

Experiments are performed in a return-style wind tunnel facility with a 9:1 contraction ratio at Portland State University. A model wind farm composed of a 4×3 array is employed wherein three model turbines are present in the cross-stream direction in each for the four rows as shown in Figure 2(a). Stereo particle image velocimetry (PIV) planes are measured

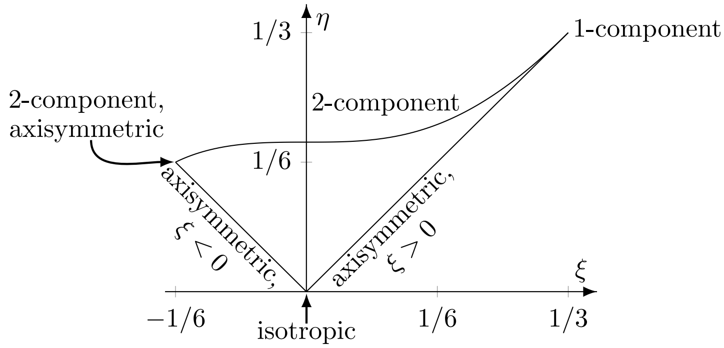

FIG. 1. The Lumley triangle with annotations showing significant regions of interest.

surrounding the center turbine in the fourth row with 3000 image pairs per dataset. Six planes are measured each with a height of approximately 240 mm in the wall normal direction and a width of approximately 165 mm in the streamwise direction. Images are processed a multi-grid strategy with two passes with interrogation area of 64 $\times$ 64 pixels followed by three passes of 32 $\times$ 32 pixels.

Measurements are done for a case in which all model turbines are fitted with three-bladed rotors and a second case in which all turbines have porous disks. Both the rotors and disks have a diameter (D) of 120 mm with drawings shown in Figure 2(b) and Figure 2(c), respectively. At hub height, the upstream edge of the rotors and porous disks are in identical streamwise positions when placed on the model nacelle. Comparing with field scales, dynamic similarity is not met making the detailed blade interactions difficult to represent due to a disparity in scales yet here the focus is on the large-scale turbulence transport properties, where Reynolds number effects are less important. Characterization of the rotor and disk characteristics is done in the first row of the array where the tip speed ratio is 3.1 and Reynolds number based on the hub height velocity and the rotor diameter is $\mathrm{Re}_D = 3.72 \times 10^4$. Thus, Re_D is on the same order of magnitude of the Reynolds number independent range found by Chamorro *et al.* [44]. Notably, the comparison of the rotor and disk cases is done utilizing to the same conditions. The model rotor and disk are matched in terms of their axial induction factor such that the axial induction factor is 0.200 and 0.202 for the rotor and disk, respectively. The axial induction factor of the rotor and disk are matched to within 1%. Full experimental details and characterization can be found in Camp *et al.* [14].

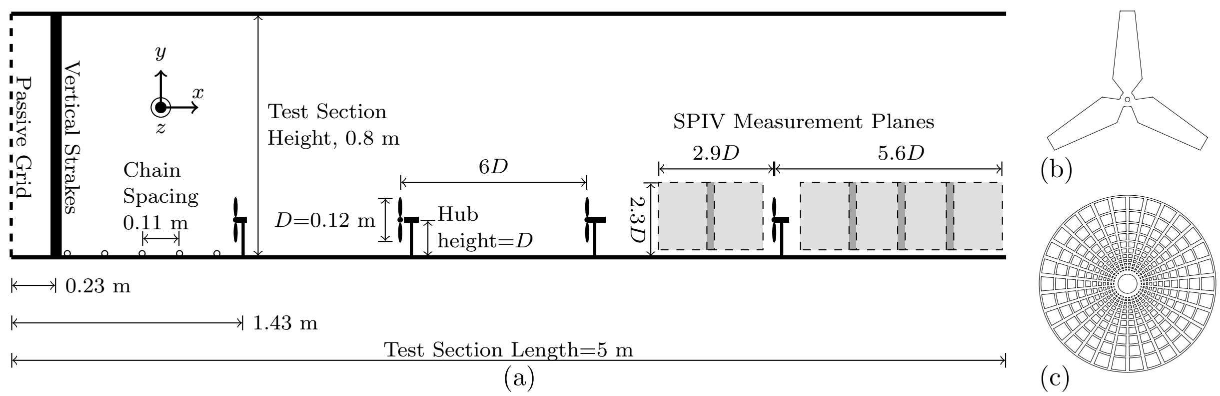

FIG. 2. Experimental setup and turbine models. (a) side view of wind tunnel test section, (b) model rotor, (c) porous disk.

IV. RESULTS AND DISCUSSION

A. Time-averaged velocity, Reynolds stresses, and turbulence kinetic energy

The normalized time-averaged statistics for the mean streamwise and spanwise velocity components, turbulence kinetic energy, and two Reynolds shear stresses are shown in Figure 3. Each subfigure is composed of four panels with the top two panels representing the flow field upstream and downstream of the rotor in the fourth row of the model farm. The bottom two panels illustrate the corresponding information for the disk case. The hub of each model turbine is located at a wall-normal height of $y/D = 1$ with the bottom tip of the rotor and disk located at $y/D = 0.5$ and top tip at $y/D = 1.5$. The streamwise location of both the rotor and the disk in the fourth row of the array is $x/D = 0$. Only a brief description of the time averaged velocity and Reynolds stresses us presented here while a more detailed discussion of these statistics and how they pertain to mean kinetic energy flux can be found in Camp *et al.* [14].

Upstream of both the rotor and disk, particularly for $x/D < -1.5$, a streamwise velocity deficit originating from the wake of the third row of turbines is evident in Figure 3(a). Immediately downstream of both turbine models, a velocity deficit is present although the rotor has a greater deficit than the disk case at hub height and $x/D = 0.6$. By $x/D = 1.5$, the hub height streamwise velocity of the rotor case is within 10% of the disk case. The streamwise velocity components between the two cases are comparable owing to the matched

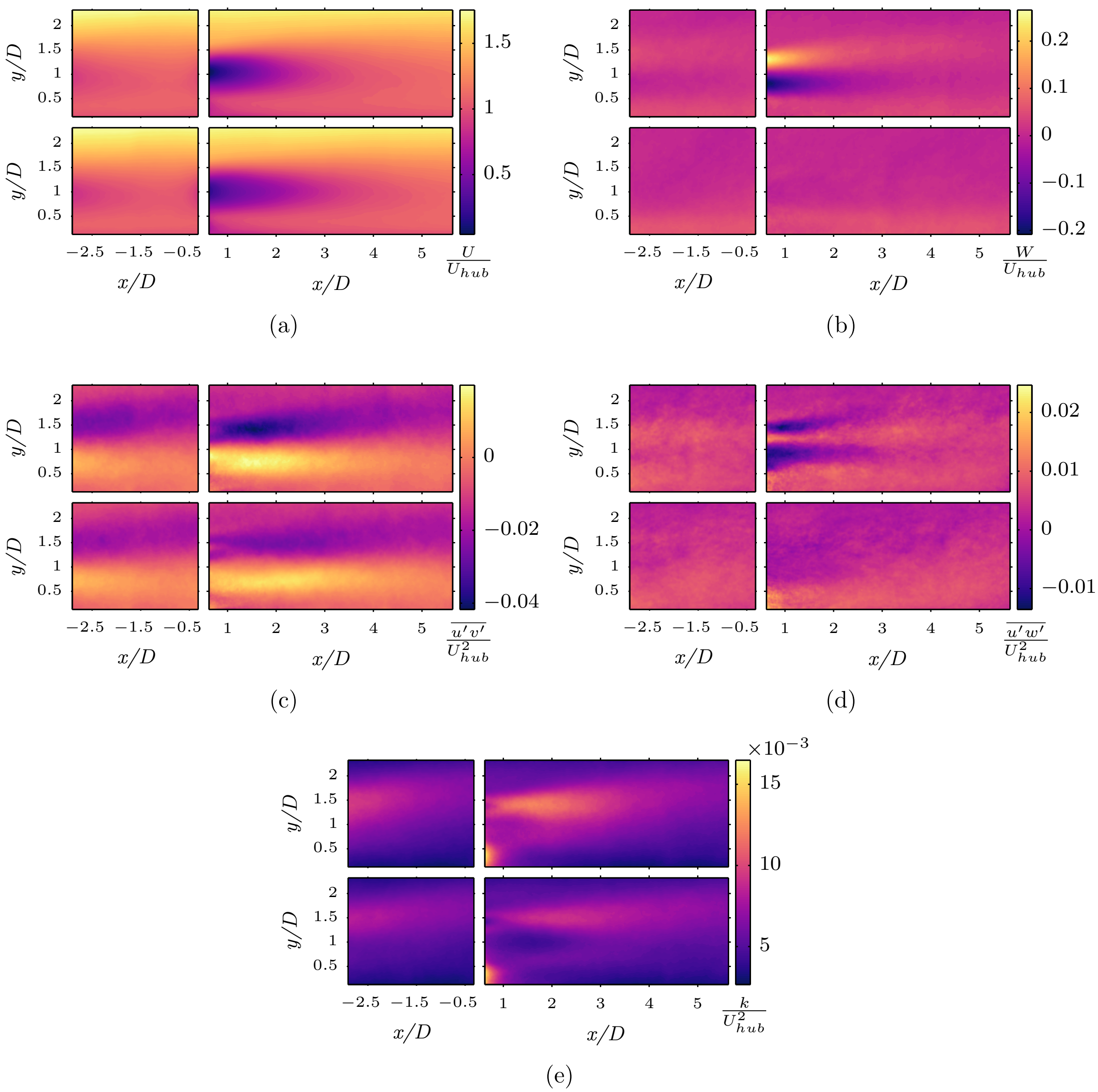

FIG. 3. Normalized time-averaged statistics of the rotor and disk cases for (a) the normalized streamwise velocity, U/U_{hub}, (b) the normalized spanwise mean velocity, W/U_{hub}, (c) the normalized in-plane Reynolds shear stress, $\overline{u'v'}/U_{hub}^2$, (d) the normalized out-of-plane Reynolds shear stress, $\overline{u'w'}/U_{hub}^2$, and (e) the normalized turbulence kinetic energy, k/U_{hub}^2. In each subfigure, the top row of two panels represent the rotor and bottom row of two panels depict the same information for the disk case.

induction factor between the rotor and disk. In contrast, the spanwise velocity component illustrated in Figure 3(b) shows dramatic qualitative and quantitative differences between the two cases with the rotor exhibiting significant out-of-plane motion due blade rotation and disk flow field showing the absence of such motion. The spanwise component are up to 190% different at $x/D = 0.6$.

The in-plane Reynolds shear stress $\overline{u'v'}/U_{hub}^2$ is qualitatively comparable between the rotor and disk cases with the rotor case exhibiting a larger magnitude of this quantity particularly at the bottom and top tip. Differences in $\overline{u'v'}/U_{hub}^2$ are especially relevant since it is known that this quantity is related to the vertical entrainment of kinetic energy [45] and previous work has found stationary disks have a different mechanism of vertical entrainment of mean kinetic energy than rotors [14]. In contrast to the similar patterns found between the two cases in $\overline{u'v'}/U_{hub}^2$, Figure 3(d) illustrates that the sign of $\overline{u'w'}/U_{hub}^2$ varies within the swept area of the rotor while no such pattern is evident in the disk case.

Figure 3(e) compares the turbulence kinetic energy, k, for the rotor and disk cases. Recalling that k is half of the trace of the Reynolds stress tensor, the similarities and disparities in k between the rotor and disk cases arise from the normal Reynolds stresses themselves. Both cases exhibit elevated values of k at the top tip as well as at streamwise distances of $x/D \leq 1$ and wall normal heights of $y/D \leq 0.5$. The latter region arises from the effects of the model turbine tower. At all streamwise distances, the magnitude of k for the two cases are less than 15% different at wall normal heights below the bottom tip. Between the top and bottom tip, the rotor case exhibits higher values of k particularly for $x/D \leq 3$. The maximum percent difference between the two cases is 62% and is found at $x/D = 1.8$ and $y/D = 1.1$. At this location, the larger normal Reynolds stresses of the rotor contribute roughly equally to the discrepancy between the two cases in k. Since the turbulence kinetic energy of each POD mode is expressed by its eigenvalue, additional comments regarding the the distribution of k amongst the POD modes are discussed in §IV C.

B. Analysis of the Reynolds stress anisotropy tensor of the mean flow field

Figure 4 shows the invariants of the normalized Reynolds stress anisotropy tensor, η and ξ, as well as the anisotropy factor, F, computed from the time-averaged Reynolds stress tensor. In Figure 4, as with the time-averaged statistics in Figure 3, the rotor case is shown in the top two panels while the disk case is shown in the bottom two panels of each subfigure. For η, ξ, and F, the primary differences between the rotor and disk cases lay in the magnitudes of each quantity while many of the overall characteristics are alike.

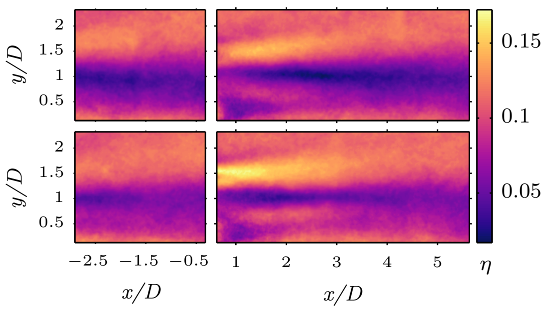

(a)

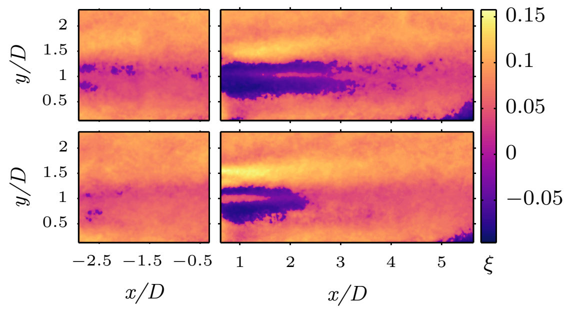

(b)

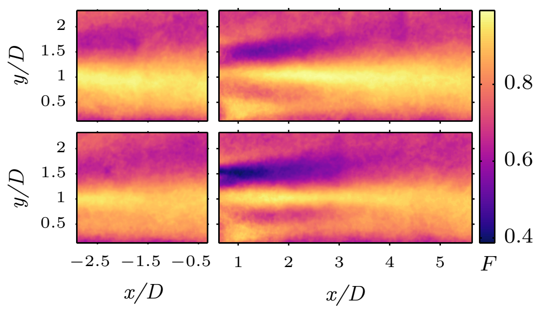

(c)

FIG. 4. Invariants of the normalized Reynolds stress anisotropy tensor and the anisotropy factor calculated from the time-averaged Reynolds stresses. (a) Second invariant η, (b) third invariant ξ, and (c) aniosotropy factor F. In all subfigures, the rotor case is shown in the top row of panels while the disk case is represented in the bottom row of panels.

In Figure 4(a), both the rotor and disk cases exhibit a low anisotropy region at hub height through the entire length of the measurement domain with the corresponding low anisotropy feature at $x/D \leq -1.5$ trailing the third row nacelle of the center third row turbine. The persistence of this reduced anisotropy feature can be also be seen in the incoming flow ($x/D < 0$) which arises from the third row. Although the disk case initially has a more significant streamwise gradient of η reaching a minimum of $\eta = 0.03$ at $x/D = 1.7$, the rotor case has a more extreme minimum of $\eta = 0.02$ at $x/D = 2.7$. For both cases, the most highly anisotropic area is found to be trailing the top tip. The lower anisotropy of the rotor case relative to the disk is consistent with the notion that the blade passage through the measurement plane is intermittent and when it is absent, the relatively isotropic inflow advects into the measurement plane. Thus, on average the flow at the height of the top tip would be expected to be lower in the rotor case than in the case of a stationary porous disk which presents a constant disturbance to the flow.

The third invariant of b_{ij} is illustrated in Figure 4(b). The rotor and disk cases both exhibit negative values of ξ surrounding hub height in the near wake indicating that there is one dominant principal component of the tensor. In the rotor case, this region extends further downstream and becomes less evident by $x/D \approx 3.5$. For the disk case, this area with $\xi < 0$ becomes less evident by $x/D \approx 2.3$ which is closer to the turbine than in the rotor case. Hamilton *et al.*, when comparing turbines with rotors that rotated in differing senses of direction, found an analogous feature downstream of the nacelle [41]. Hamilton *et al.* also established that the shape of the region with $\xi < 0$ differed depending on the direction of rotation of the rotor which is consistent with the varying shape of this region in the rotor and disk cases. Trailing the turbine top tip, the rotor and disk case both exhibit elevated values of ξ with $\xi > 0$ indicating two co-dominant principal components of the corresponding tensor. However, the maximum for the disk case is larger in magnitude by 13% percent in comparison to the rotor case and this maximum occurs closer to the disk in terms of streamwise distance.

Figure 4(c) depicts the anisotropy factor for the rotor and disk cases. Since the computation of F includes both η and ξ, the features of F reflects the characteristics discussed in relation to Figure 4(a) and Figure 4(b). Namely, the rotor and disk cases both exhibit a highly anisotropic feature trailing the top tip in the near wake with an isotropic region downstream of the nacelle which persists for the extent of the wake measured. In contrast to the near wake, the far wake shows comparatively homogeneous values of F.

Lumley triangles of the second and third invariants for the time-averaged statistics for the rotor and disk case are given in Figure 5. Points are colored based on the wall-normal coordinate with black representing small values of y/D near the floor and yellow representing the highest wall normal coordinate. The left column of this figure corresponds to the rotor case while the right column represents the disk case.

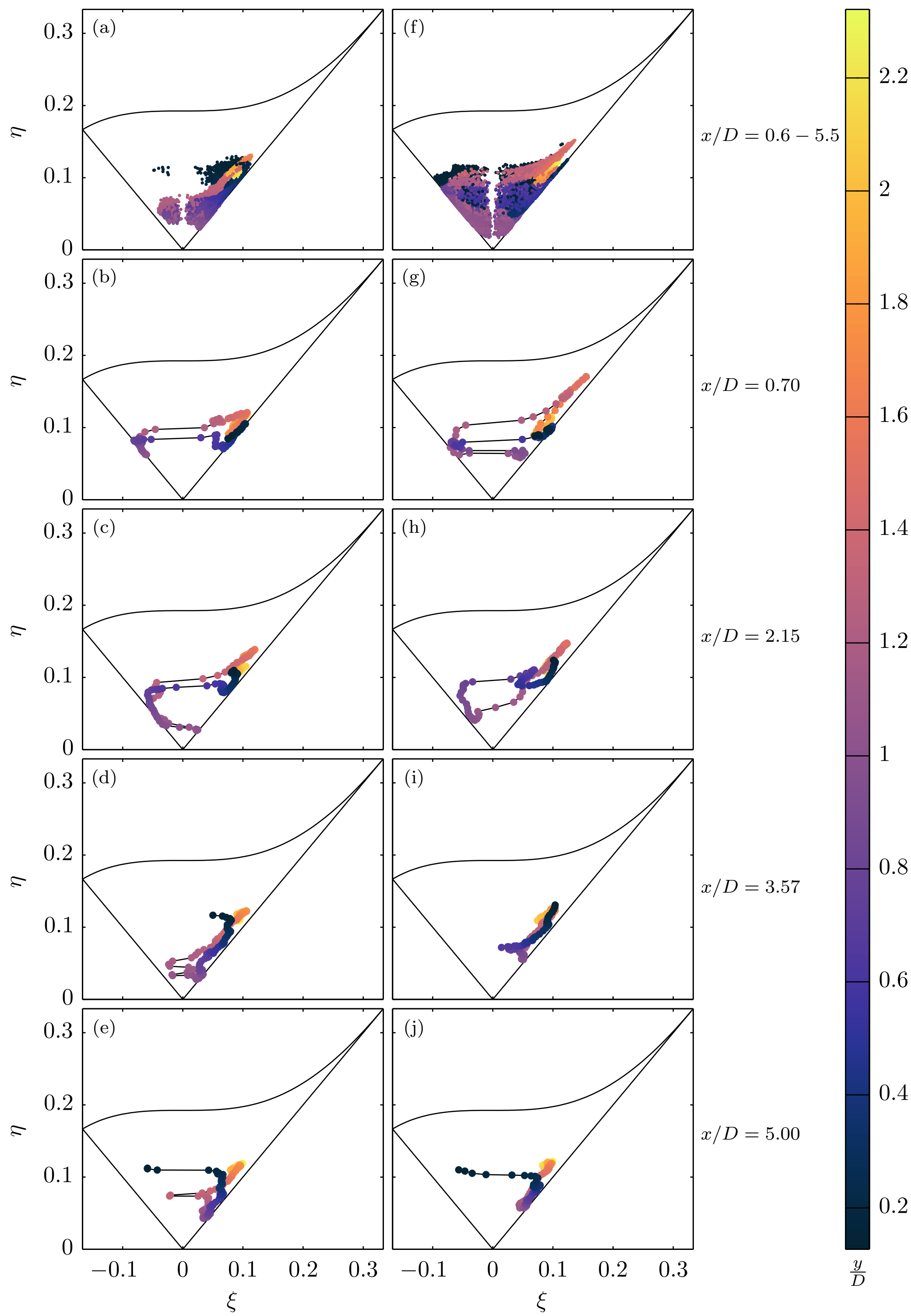

FIG. 5. Anisotropy invariant maps computed from the time-averaged Reynolds stress anisotropy tensor for $0.6 \leq x/D \leq 5.6$ with points shaded by wall-normal distance. (a) all points measured for rotor $0.6 \leq x/D \leq 5.6$, (b)-(e) profiles for the rotor case, (f) all points measured for the disk $0.6 \leq x/D \leq 5.6$, and (g)-(j) profiles for the disk case.

The AIMs of the overall wake of the rotor and disk cases are compared in Figure 5(a) and Figure 5(f), respectively. The disk case shows a larger domain and range of values in the AIM than the rotor case, a result that is not as obvious when viewing the invariants on contour maps as in Figure 4. Evident in the global version of the AIM, but further illustrated in the profiles of the near wake shown in Figure 5(b) and Figure 5(g), is an anisotropic region at $y/D \approx 1.5$ corresponding to the top tip close to the axisymmetric boundary for $\xi > 0$. Notably, the values of η for the disk case in Figure 5 are greater than those of the rotor case. Another feature more apparent in the AIM profiles than in the contour maps is the large values of η for locations below the bottom tip near the floor which are shaded dark blue and black. The relatively anisotropic flow near the floor is in accordance with observations in channel flows indicating than anisotropy is generally greater approaching the wall [32]. Comparing profiles in Figure 5, one observes that as streamwise coordinate increases, points in the profiles tend to more closely follow the positive axisymmetric boundary of the Lumley triangle.

C. Snapshot proper orthogonal decomposition of the near and far wake

Each dataset is composed of 3000 velocity fields and since the POD kernel is comprised of 3000 velocity snapshots, there are 3000 POD modes that result per dataset. Each POD mode is associated with an eigenvalue that represents the spatial average of the turbulence kinetic energy in the mode. Given that two measurement planes were analyzed via POD and datasets for the rotor and disk case are present for each plane, a total of four sets of POD results are considered herein.

Figure 6 shows the eigenvalues for the POD in each selected case normalized by the sum of the eigenvalues. Note that the sum of all eigenvalues represents the spatial average of the ensemble-averaged TKE in each measurement domain. POD modes are sorted in terms of their TKE as represented by their respective eigenvalues. However, since larger scale structures contain more energy than smaller scale structures, POD modes can generally be taken to be sorted from larger to smaller scale as well.

The cumulative sum of all 3000 modes normalized the sum of the eigenvalues is illustrated in Figure 6(a). The most evident difference between the cases is in the rate of convergence in the near wake in comparison to the far wake. The slower rate of convergence of the near

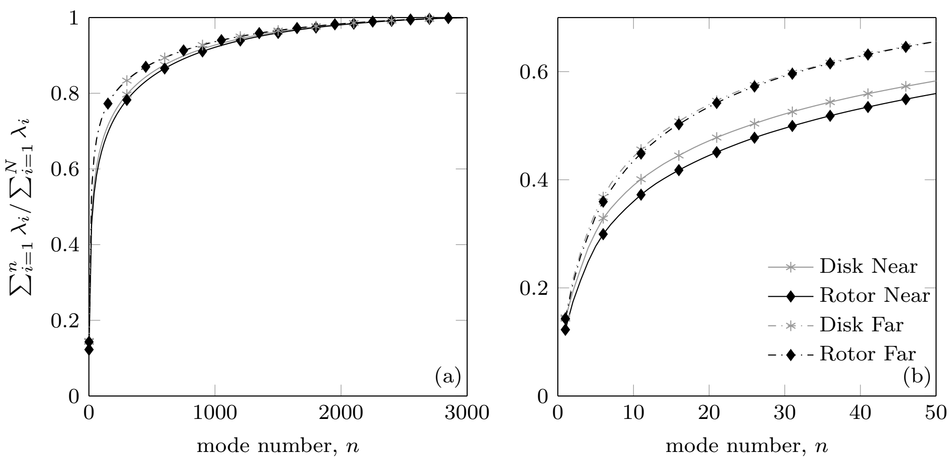

FIG. 6. Eigenvalues for the snapshot POD in the near wake ($0.6 \leq x/D \leq 2.0$) and far wake ($4.2 \leq x/D \leq 5.6$) for the rotor as well as disk cases. (a) Cumulative sum of eigenvalues for all 3000 modes normalized by the sum of all eigenvalues and (b) detailed view of cumulative sum of eigenvalues for 50 modes normalized by the sum of all eigenvalues.

wake cases is consistent with the idea that there is a larger amount of energy and importance on intermediate scales in the near wake. In contrast, a greater proportion of energy would be expected to be present in larger scales in the far wake cases based on the rate of convergence shown in Figure 6(a) and fewer modes are required to recover the dynamics of the flow than in the near wake cases.

In order to focus on the behavior of low rank modes, the cumulative summation of only the first 50 modes normalized by the total of all eigenvalues is provided in Figure 6(b). Only an insignificant difference in the rate of convergence is present between the disk and rotor cases in the far wake. Meanwhile, the discrepancy between the rotor and disk case is more evident in the near wake. The smaller gradient of the curve in the rotor case suggests the greater emphasis on intermediate scales than in the disk case. Different gradients in the rotor and disk cases in the near wake also implies that flow is more complex in the rotor case and that a greater number of degrees of freedom are needed to represent the full dynamic behavior of the flow in the rotor case than in the disk case in the near wake.

Selected POD modes are presented in Figure 7 in order to illustrate the structural differences in modes amongst the test cases as well as how these features vary with the mode index. The kernel of the POD in the present work includes fluctuations in the streamwise, wall-normal, and spanwise directions. Thus, the resulting POD modes ($\mathbf{\Phi}$) have a

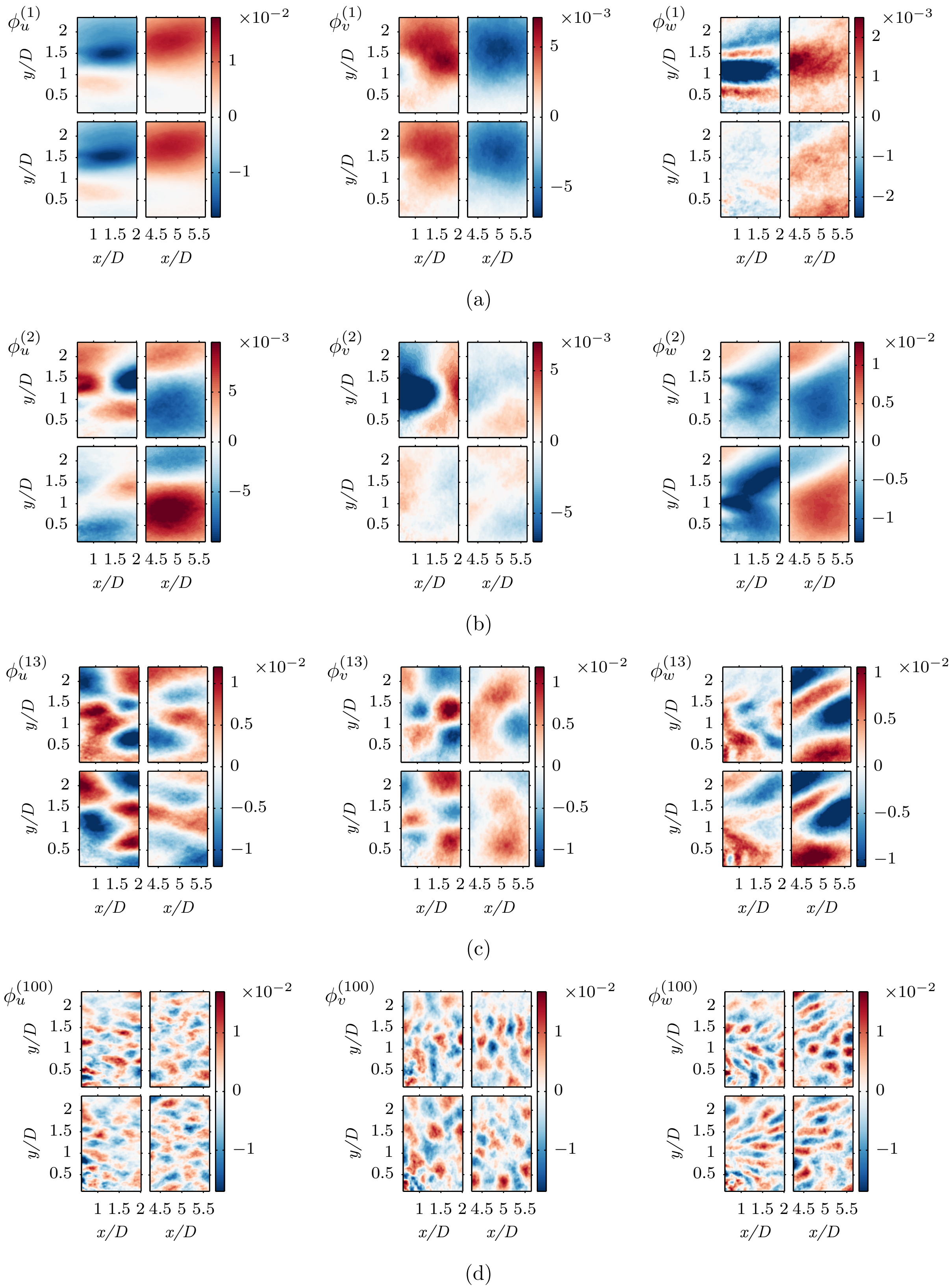

FIG. 7. Vectorial components ϕ_u, ϕ_v, and ϕ_w of selected POD modes. (a) POD mode 1, (b) POD mode 2, (c) POD mode 13, and (d) POD mode 100. Four contour maps illustrate each vectorial component with the top row of panels in each component representing the rotor case and the bottom row of each component depicting the disk case.

streamwise component (ϕ_u), wall-normal component (ϕ_v), and spanwise component (ϕ_w). In Figure 7, each component of a given POD mode is illustrated via four panels in which the top two panels correspond to the near and far wake of the rotor case while the bottom row of two panels correspond to the near and far wake of the disk case. While all panels of a given component are shown on the same scale, the color scale is unitless. Furthermore, the numerical value of the color scale lacks physical meaning since it is only the combination of a mode with the corresponding time-dependent coefficient yields a velocity field (see Eqn (1) in §II).

Overall, Figure 7 illustrates a trend toward smaller scale features as the mode index increases. For example, comparing the components of $\Phi^{(1)}$ to those of $\Phi^{(100)}$, the features of $\Phi^{(1)}$ are on the order of the measurement domain while those found $\Phi^{(100)}$ are about an order of magnitude smaller in size. However, length scales cannot be strictly computed directly from spatial POD modes. Nevertheless, the reduction in feature size is in accordance with the expectation that although POD sorts modes based on energetic content, such sorting also has the effect of ordering by scale since larger scales generally contain more energy.

The u- and v-components of the first POD mode of the rotor and disk cases, shown in Figure 7(a), are consistent with one another in both the near and the far wake measurement domains. In the near wake as well as in the far wake in both the rotor and the disk cases, $\phi_u^{(1)}$ displays a prominent feature near the top tip which is also reflected in $\overline{u'u'}$ and $\overline{u'v'}$. In contrast to the comparable nature of the inplane components of $\Phi^{(1)}$, $\phi_w^{(1)}$ displays clear organization in the near wake of the rotor case which results from the rotation of the rotor. No such clear structure is present in $\phi_w^{(1)}$ in the near wake of the disk case. Furthermore, $\phi_w^{(n)}$ retains a degree of coherence in the rotor case into the far wake while the disk case continues to lack clear organization. The coherence of $\phi_w^{(1)}$ in the far wake of the rotor case is notable given that rotor and disk wakes are often considered to be equivalent in the far wake in the literature (e.g., see [13], [14]).

Evident in Figure 7(b) and Figure 7(c) is the tendency for components of modes at the same location and mode index to be antisymmetric with respect to the sign of $\phi_i^{(n)}$. For example, comparing $\phi_u^{(2)}$ in the far wake there is a zero crossing at about the top tip for the rotor as well as the disk case and this component otherwise displays comparable topology albeit with the signs reversed in the far wake. A similar comparison can be made between the rotor and disk cases for the far wake of $\phi_w^{(2)}$ as well as the far wake of $\phi_u^{(2)}$ and the same reversing of sign can be observed. The sign ascribed to a particular point in a mode is arbitrary. The contribution of a mode to the fluctuating velocity field is determined by the combination of Φ_n with the corresponding time-dependent coefficient a_n. Since the sign of $\Phi^{(n)}$ can be negated by a_n, antisymmetrical modes can be considered to be equivalent. Thus, antisymmetrical modes such as those found in the far wake of $\phi_w^{(2)}$ can be considered to have an analogous structure and contribute the same features to the velocity field upon reconstruction.

Apparent in Figure 7(c) is onset of the loss of common projections between the modes of the rotor and disk cases. By $n \approx 17$ such behavior is common and modes of the same index and at the same location often have differing topological characteristics. Notable in $\phi_w^{(13)}$ is a set of small stripes of opposing sign below the bottom tip and at streamwise distances of $x/D \leq 1.3$. Similar stripes, which are often out of phase by a fraction of a wavelength in comparison to those illustrated in $\phi_w^{(13)}$, are common in the out-of-plane component of low rank modes. The location as well as the phase-shifting behavior of these stripes is consistent with vortex shedding that would be anticipated to be present downstream of a bluff body such as the turbine tower. That these features do not extend upward into the swept area of the turbine is significant since flow structures shed by the turbine tower would be expected to be overwhelmed by the presence of a rotor or a disk.

Common to the discussion of the first- and second-order statistics of the time-averaged velocity field in §IV A and the discussion the POD modes shown in Figure 7 is the observation that the out-of-plane characteristics of the flow fields of the rotor and the disk are significantly different due to the rotation of the rotor. In a similar vein, a key finding from Camp and Cal [14] was that the out-of-plane velocity component contributed in considerably disparate ways to the vertical entrainment of mean kinetic energy when comparing a rotor and a stationary disk. In order to further probe how the out-of-plane component contributes to a particular POD mode, the energetic contribution from each velocity component to each POD mode can be found. The TKE contribution from each component to a given POD mode can be found by reconstructing the individual fluctuating velocity component $u_i'^{(n)}$ from a given single POD mode $\phi_i^{(n)}$ and the corresponding time coefficients a_n. From the reconstructed fluctuating velocity component from a single mode, the amount of TKE contained in this single component for the n^{th}single mode is denoted as $\gamma_{ij}^{(n)}$. Furthermore, $\gamma_{ij}^{(n)}$ can be expressed as

$$\gamma_{ij}^{(n)} = \frac{\left\langle \frac{1}{2}\overline{u_i'^{(n)} u_j'^{(n)}\delta_{ij}} \right\rangle_\Omega}{\langle k \rangle_\Omega}, \tag{16}$$

where $i, j = 1, 2,$ or 3 which correspond to the u-, v-, and w-components, respectively. Furthermore, $u_i'^{(n)}$ is the fluctuating velocity component in the i^{th} direction (e.g. if $i = 2$, $u_i'^{(n)} = v'^{(n)}$) reconstructed from the n^{th} POD mode, δ_{ij} is the Kronecker delta, k is the turbulence kinetic energy, and $\langle ... \rangle_\Omega$ is spatial averaging over a PIV measurement domain performed by double trapezoidal integration. In practice, $\gamma_{ij}^{(n)}$ is computed using Eqn. (8) in §II as follows

$$\gamma_{ij}^{(n)} = \frac{\left\langle \frac{1}{2}\overline{a_n^2 \phi_i^{(n)} \phi_j^{(n)}}\delta_{ij} \right\rangle_\Omega}{\sum_{m=1}^{N} \lambda_m}. \tag{17}$$

Note that only cases where $i = j$ are nonzero due to δ_{ij}. Furthermore, the sum of all $\gamma_{ij}^{(n)}$ for a given mode index, n, is equal to $\lambda_n / \sum_{m=1}^{N} \lambda_m$ for that same mode index.

Figure 8 shows the variation of the TKE from each fluctuating velocity component, $\gamma_{ij}^{(n)}$, for modes 1 through 15. The top row of subfigures in Figure 8 represents the rotor near and far wake while the bottom row of subfigures illustrates the corresponding results for the disk case. In each case, $\gamma_{11}^{(1)}$ is much greater than the $\gamma_{22}^{(1)}$ or $\gamma_{33}^{(1)}$ indicating that the u-component is the dominant contributer to the TKE for the first mode which explains the strong resemblance observed in the spatial organization of $\phi_u^{(1)}$ in Figure 7(a) with that of $\overline{u'u'}$ in Figure 3. Not only do low rank modes in the near wake of the rotor display the expected substantial contributions from the out-of-plane component, remarkably, the w-component is a primary contributer to the TKE of $\Phi^{(2)}$ in the near wake of the disk case as seen in Figure 8(b) indicating that the stationary disk near wake contains large scale organization in which the out-of-plane component is of prime importance. Furthermore, large scale organization that involves the w-component remains in the far wake in both the rotor and disk cases as is apparent from the magnitude of $\gamma_{33}^{(2)}$ as well as $\gamma_{33}^{(3)}$ in 8(b) and 8(d). While differences in the relative energetic contributions from each velocity component are evident in the near wake when comparing the rotor and disk, such discrepancies are diminished in the far wake.

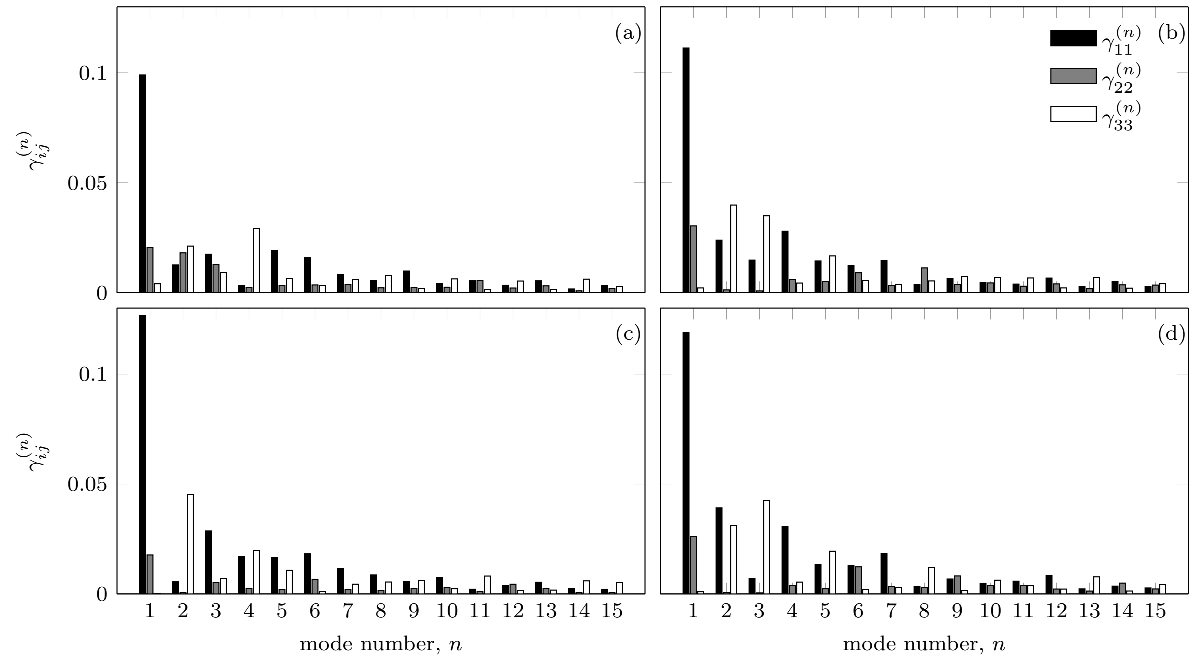

FIG. 8. Turbulence kinetic energy from each component of the fluctuating velocity, $\gamma_{ij}^{(n)}$, where the component i, j = 1, 2, or 3 for each mode n. (a) rotor near wake measurement plane, (b) rotor far wake measurement plane, (c) disk near wake measurement plane, and (d) disk far wake measurement plane. The near wake measurement plane is $0.6 \leq x/D \leq 2.0$ and the far wake measurement plane is $4.2 \leq x/D \leq 5.6$ which are the same planes provided for the POD spatial eigenfunctions.

D. Invariants of low-dimensional reconstructions of the Reynolds stress tensor

The anisotropy of the Reynolds stress tensor and its invariants are used in §IV B to gain detailed insight into the similarities and differences between the rotor and disk cases as a function of spatial location. In the same way, the Reynolds stress tensor can be reconstructed from a subset of POD modes and the resulting anisotropy invariants can be computed to provide additional understanding of the character of the POD modes utilized in the reconstruction. The same four cases analyzed via POD and discussed in §IV C, which includes the rotor and disk case in the near wake ($0.6 \leq x/D \leq 2.0$) and far wake ($4.2 \leq x/D \leq 5.6$), are considered. The analysis procedure used involved first choosing a subset of POD modes with indices 1 to S and the Reynolds stress tensor is then reconstructed using modes 1 to S utilizing Eq. 9. The reconstructed normalized Reynolds stress anisotropy tensor is then formulated and finally the invariants of the reconstructed normalized Reynolds stress anisotropy tensor are found. The procedure can then repeated after increasing the number of modes in the subset to be analyzed.

An overview of the features of the invariants that occur commonly in all four cases as S is allowed to increase are highlighted using selected of values of S in Figure 9. The subset where $S = 2$, which is a reconstruction using only POD modes 1 and 2, yields anisotropy invariants on the 2-component boundary of the Lumley Triangle. As the number of modes in the subset is increased to $S > 2$, the invariants descend from the 2-component boundary as can be seen when the number of modes is increased to $S = 6$. When the subset includes only a small number of POD modes, rapid changes in the invariants of the reconstructed anisotropy tensor are observed. As the number of modes in the subset is increased, some modes cause the invariants of the reconstructed anisotropy tensor to diverge from its final value as is observed when comparing the sequence where $S = 2$ is increased to $S = 6$ and then to $S = 12$. However, the general trend as the value of S increases, which corresponds to additional modes used in the reconstruction of the normalized Reynolds stress anisotropy tensor, is a decrease in the magnitude of η.

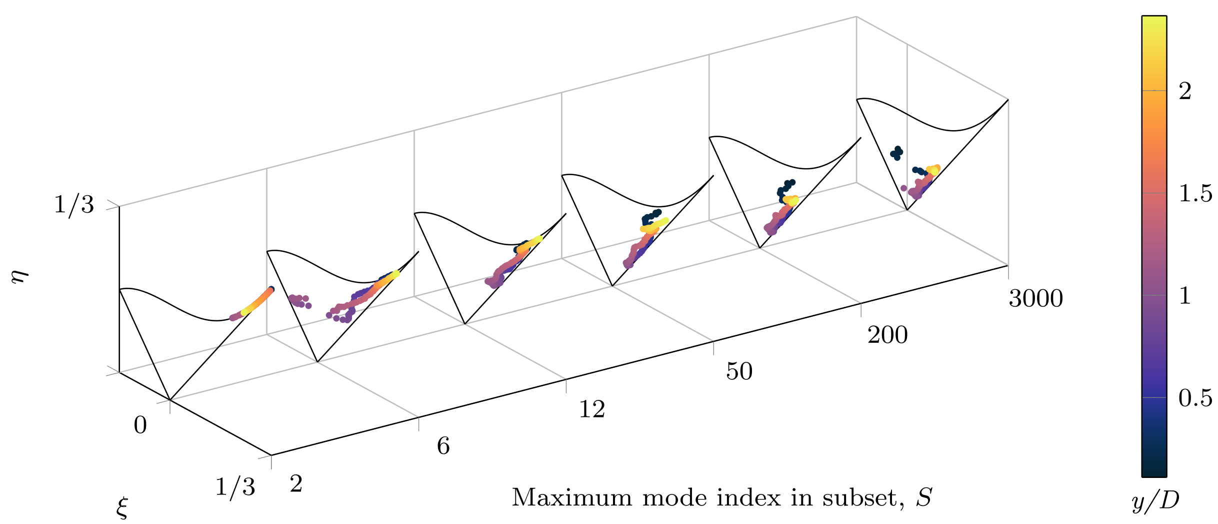

FIG. 9. Representative Lumley triangles from POD reconstructions of the normalized Reynolds stress anisotropy tensor using modes 1 to S where S is increased from 2, 6, 12, 50, 200 and finally the full basis of 3000. The POD was applied over a plane in the far wake ($4.2 \leq x/D \leq 5.6$) of the rotor case and invariants for each reconstruction were selected at $x/D = 5.00$.

Figure 10 gives a more detailed comparison of the anisotropy of the rotor and disk in the near and far wake as a function of the number of POD modes used to reconstruct the normalized Reynolds stress anisotropy tensor. Every subset is examined wherein the reconstruction was performed with modes 1 to S where S is allowed to increase in increments of one from $S = 1$ to $S = 3000$, where 3000 represents the full basis. The value of F is integrated over each measurement plane for each reconstruction to arrive at a single scalar, $\langle F \rangle|_S$, that expresses the anisotropic character of the each reconstruction. The eigenvalues and spatial eigenfunctions of these measurement planes are discussed in §IV C. Thus, the integration to arrive at $\langle F \rangle|_S$ allows a more compact view of the information of the type presented in Figure 9 recalling that $F = 1 - 27\eta^2 + 54\xi^3$.

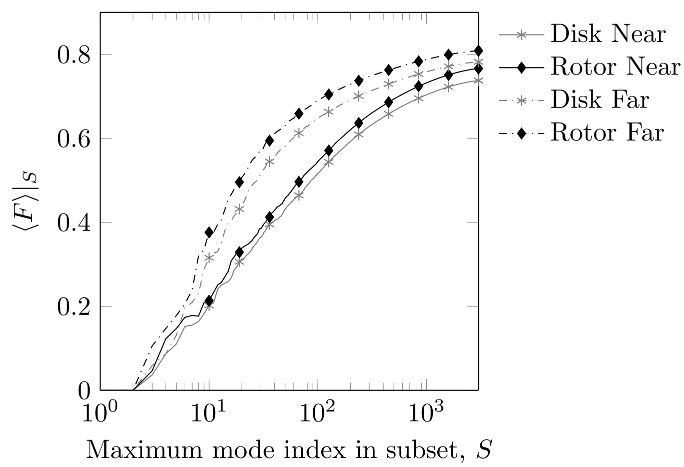

FIG. 10. Spatially integrated anisotropy factor, $\langle F \rangle|_S$, computed from POD reconstructions using modes 1 to S where S varies from 1 to the full basis of 3000. Spatial integration was done on the POD of a plane in the near wake ($0.6 \leq x/D \leq 2.0$) and the far wake ($4.2 \leq x/D \leq 5.6$) of the both the rotor and disk cases. The corresponding POD eigenvalues and spatial eigenfunctions for these cases are discussed in §IV C.

Both Figure 9 and Figure 10 show that the reconstructed velocity field has a high degree of anisotropy as reflected by the anisotropy invariants. Such a result is consistent with the previous literature wherein Hamilton *et al.* [46] demonstrated that reconstructions using only the single lowest rank POD mode resulted in 1-component turbulence. Thus, the small values of $\langle F \rangle|_S$ for reconstructions using a severely truncated basis of POD modes should be viewed as an indication both of the high degree of anisotropy of the large scale structures described by these modes as well as the influence of basis truncation.

E. Conclusions

The wake of a model turbine fitted with a three-bladed rotor is compared to the wake of a model turbine fitted with a matched stationary porous disk for the turbine in the fourth row of a 4×3 wind turbine array. Wake characteristics are particularly critical in the function of wind farms since most turbines in wind farms operate within the wake of turbines located upstream. The present experimental comparison sheds light on the similarities and differences between the wake produced by stationary rotor parameterizations often employed in computational studies and the wake issuing from the rotating rotor that these parameterizations seek to model. The experimental work described herein allows for an unbiased approach that circumvents the difficulties that arise when this comparison is done via a joint computational and experimental study. The similarities and differences between the wake of a rotor and disk within a turbine array are examined via the first and second order statistics of the time-averaged velocity field and through the invariants of the normalized Reynolds stress anisotropy tensor. Furthermore, the rotor and disk are compared by the application of proper orthogonal decomposition (POD) and finally by examining the anisotropic character for the stress tensor resulting from POD reconstruction.

The most notable differences in the first and second order statistics of the velocity fields of the rotor and disk were found to be in quantities that include the spanwise velocity component that arises from the rotation of the rotor. Second order statistics, which describe the fluctuations about the mean, are consistently higher in the rotor wake. The discrepancies in $\overline{u'v'}$ between the rotor and disk wake are particularly relevant to the vertical entrainment of mean kinetic energy which is the main source of energy that fosters recovery of the wake deficit in wind turbine arrays[45]. The larger values of $\overline{u'v'}$ in the rotor case at both the top and bottom tip suggest that greater flux of mean kinetic energy is present in rotor case than the disk case particularly in the near wake. Such a finding is relevant to modeling studies that examine quantities relating to energy entrainment such as power. Previous work has provided a detailed comparison of the mean kinetic energy exchange within the wake of disks versus rotors [14].

Characterization of the invariants of the normalized Reynolds stress anisotropy tensor of the time-averaged flow field illustrate a remarkably higher level of anisotropy at the top tip in the disk case as indicated by a difference of 13% in η. Such a surprising result is consistent with the intermittent presence of the rotor in the measurement plane in contrast with the fixed nature of the disk. While this difference at the top tip becomes insignificant for $x/D \geq 3.2$, disparities in the value of η and ξ trailing the nacelle persist into far wake. Physically, the differences in the spatial distribution of the anisotropy tensor invariants between the two cases reflects that the balance of the components in the turbulence kinetic energy tensor as well as the evolution of this balance differs in the disk versus rotor wake. When the invariants are displayed on a Lumley Triangle, the larger range and domain of η and ξ in the disk case becomes apparent in comparison to the more tightly clustered values of η and ξ in the rotor case.

The snapshot POD was performed in selected segments of the near wake as well as the far wake for the rotor and disk cases. While the distribution of energy of the disk mirrors that of the rotor in the far wake, the rate of convergence of the turbulence kinetic energy is slower in the rotor case than the disk case. This reduction in the convergence rate in the near wake of the rotor case implies that intermediate scales carry a greater energetic importance in the rotor case. Furthermore, when comparing the near wake and far wake more emphasis is placed on these intermediate scales in general. Such a change in the significance of certain scales is relevant from a practical perspective in wind farms since the acoustics of flow over the rotors is impacted by the scales of the incoming flow [47, 48]. The unfavorable acoustic impact of wind farms continues to be a contentious issue in the implementation of wind turbine arrays.

The POD describes the basis for the structure of the flow that is optimal in terms of energy content. The topology of the spatial POD modes Φ of the rotor and the disk were compared in the near and the far wake. While the components of many low rank modes were comparable, the spanwise component of the rotor case in mode 1 ($\phi_w^{(1)}$) displayed large scale spatial organization in the near wake and retained its coherence in the far wake while the disk case showed no such organization. Differences in the scales and structure of the wakes found via the POD demonstrate that care should be used when employing a stationary disk model in place of a rotating model in studies pertaining to wind turbine arrays where turbine structural behavior is sought particularly for those turbines operating in the wakes of upstream turbines. The fatigue behavior of turbines is known to be tied to the structure of the inflow [4, 5] and is dependent on the scales within the inflow [6]. Thus, the results of the POD described herein suggest that fatigue prediction from aeroelastic simulations utilizing a disk parametrization could be unrepresentative what would be found if rotation was more adequately modeled due to the scales and structure of the wake advected from upstream turbines.

Reconstructing the normalized Reynolds stress anisotropy tensor from the entire sequence of subsets of POD modes provided insight as to the dependence of flow anisotropy on the POD basis used in the reconstruction. Reconstructions done using only the low rank modes are highly anisotropic based on the value of $\langle F \rangle|_S$ however these elevated values of $\langle F \rangle|_S$ reflects both the increase in anisotropy inherent in basis truncation and also reflects the high levels of anisotropy that are characteristic of large scale flow structures. Interestingly, as the number of modes in the subset used to reconstruct the flow field increases, the residual between the subset and the full basis using 3000 modes did not monotonically decrease. However, such behavior was only observed when reconstructions were performed using low rank modes.

The vertical mean kinetic energy entrainment characteristics of wakes of rotors and stationary porous disks have been previously studied and have determined that while significant disparities between the mechanism of mean kinetic energy entrainment in the rotor and disk was present in the near wake, the two cases were comparable in the far wake [14]. However, the present work provides new insight into the separate issue of the structural features of the turbulent field inherent in these wakes. An encouraging degree of resemblance was found in the spatial organization of the low rank POD modes as well as the anisotropic character of the flow in the far wake. However, the discrepancy between the spanwise component of the first POD mode, differences in the distribution of energy amongst the modes, as well as differences in the anisotropic character of the turbulence in the near wake between the rotor and disk cases indicate the care should be used when a stationary disk is used to model a rotor particularly if acoustic or structural information is sought.

ACKNOWLEDGMENTS

Vasant Vuppuluri is acknowledged for his help in disk characterization and experimental set up. This work was funded by the National Science Foundation (NSF-CBET-1034581).

---

[1] Global Wind Energy Council. Global Wind Report Annual Market Update 2016. Technical report, Global Wind Energy Council, 2016.

[2] R. J. Barthelmie, S. C. Pryor, S. T. Frandsen, K. S. Hansen, J. G. Schepers, K. Rados, W. Schlez, A. Neubert, L. E. Jensen, and S. Neckelmann. Quantifying the Impact of Wind Turbine Wakes on Power Output at Offshore Wind Farms. *Journal of Atmospheric and Oceanic Technology*, 27(8):1302–1317, August 2010.

[3] J. F. Herbert-Acero, O. Probst, P.-E. Réthoré, G. C. Larsen, and K. K. Castillo-Villar. A Review of Methodological Approaches for the Design and Optimization of Wind Farms. *Energies*, 7(11):6930–7016, oct 2014.

[4] M. J. Churchfield, S. Lee, J. Michalakes, and P. J. Moriarty. A numerical study of the effects of atmospheric and wake turbulence on wind turbine dynamics. *Journal of Turbulence*, 13:N14, January 2012.

[5] S. Lee, M. Churchfield, P. Moriarty, J. Jonkman, and J. Michalakes. Atmospheric and wake turbulence impacts on wind turbine fatigue loadings. In *50th AIAA Aerospace Sciences Meeting including the New Horizons Forum and Aerospace Exposition*, pages 09–12, 2012.

[6] K. Thomsen and P. Sørensen. Fatigue loads for wind turbines operating in wakes. *Journal of Wind Engineering and Industrial Aerodynamics*, 80(12):121–136, March 1999.

[7] P.-Å. Krogstad and P. E. Eriksen. Blind test calculations of the performance and wake development for a model wind turbine. *Renewable Energy*, 50:325–333, February 2013.

[8] L. E. M. Lignarolo, D. Mehta, R. J. A. M. Stevens, A. E. Yilmaz, G. van Kuik, S. J. Andersen, C. Meneveau, C. J. Ferreira, D. Ragni, J. Meyers, G. J. W. van Bussel, and J Holierhoek. Validation of four LES and a vortex model against stereo-PIV measurements in the near wake of an actuator disc and a wind turbine. *Renewable Energy*, 94:510–523, August 2016.

[9] B. Sanderse, S. P. van der Pijl, and B. Koren. Review of computational fluid dynamics for wind turbine wake aerodynamics. *Wind Energy*, 14(7):799–819, oct 2011.

[10] Y.-T. Wu and F. Porté-Agel. Large-Eddy Simulation of Wind-Turbine Wakes: Evaluation of Turbine Parametrisations. *Boundary-Layer Meteorology*, 138(3):345–366, March 2011.

[11] L. A. Martínez-Tossas, M. J. Churchfield, and S. Leonardi. Large eddy simulations of the flow past wind turbines: actuator line and disk modeling. *Wind Energy*, 18(6):1047–1060, jun 2015.

[12] S. Aubrun, S. Loyer, P. E. Hancock, and P. Hayden. Wind turbine wake properties: Comparison between a non-rotating simplified wind turbine model and a rotating model. *Journal of Wind Engineering and Industrial Aerodynamics*, 120:1–8, sep 2013.

[13] L. E. M. Lignarolo, D. Ragni, C. J. Simo Ferreira, and G. J. W. van Bussel. Kinetic energy entrainment in wind turbine and actuator disc wakes: an experimental analysis. *Journal of Physics: Conference Series*, 524(1):012163, June 2014.

[14] E. H. Camp and R. B. Cal. Mean kinetic energy transport and event classification in a model wind turbine array versus an array of porous disks: Energy budget and octant analysis. *Physical Review Fluids*, 1(4), August 2016.

[15] G. Berkooz, P. Holmes, and J. L. Lumley. The proper orthogonal decomposition in the analysis of turbulent flows. *Annual review of fluid mechanics*, 25(1):539–575, 1993.

[16] P. Holmes, J. L. Lumley, G. Berkooz, and C. W. Rowley. *Turbulence, coherent structures, dynamical systems and symmetry.* Cambridge University Press, Cambridge, 2nd edition, 2012.

[17] J. L. Lumley. The structure of inhomogeneous turbulent flows. In *Atmospheric Turbulence and Radio Wave Propagation.* 1967. editors: A.M. Yaglom, V.I. Tartarski pp. 166-78. Moscow: Nauka.

[18] L. Sirovich. Turbulence and the dynamics of coherent structures. Part I: Coherent structures. *Quarterly of applied mathematics*, 45(3):561–571, 1987.

[19] S. J. Andersen, J. N. Sørensen, and R. Mikkelsen. Simulation of the inherent turbulence and wake interaction inside an infinitely long row of wind turbines. *Journal of Turbulence*, 14(4):1–24, April 2013.

[20] S. J. Andersen, J. N. Srensen, and R. Mikkelsen. Reduced order model of the inherent turbulence of wind turbine wakes inside an infinitely long row of turbines. *Journal of Physics: Conference Series*, 555(1):012005, 2014.

[21] C. VerHulst and C. Meneveau. Large eddy simulation study of the kinetic energy entrainment by energetic turbulent flow structures in large wind farms. *Physics of Fluids (1994-present)*,

26(2):025113, 2014.

[22] D. Bastine, B. Witha, M. Wächter, and J. Peinke. Towards a Simplified DynamicWake Model Using POD Analysis. *Energies*, 8(2):895–920, 2015.

[23] N. Hamilton, M. Tutkun, and R. B. Cal. Low-order representations of the canonical wind turbine array boundary layer via double proper orthogonal decomposition. *Physics of Fluids (1994-present)*, 28(2):025103, 2016.

[24] S. J. Andersen, J. N. Sørensen, and R. F. Mikkelsen. Turbulence and entrainment length scales in large wind farms. *Phil. Trans. R. Soc. A*, 375(2091):20160107, April 2017.

[25] J. C. Rotta. Statistische theorie nichthomogener turbulenz. *Zeitschrift fr physik*, 129(6):547–572, 1951.

[26] S. B. Pope. *Turbulent flows*. IOP Publishing, 2001.

[27] K.-S. Choi and J. L. Lumley. The return to isotropy of homogeneous turbulence. *Journal of Fluid Mechanics*, 436:59–84, June 2001.

[28] K. Horiuti. A proper velocity scale for modeling subgrid-scale eddy viscosities in large eddy simulation. *Physics of Fluids A: Fluid Dynamics*, 5(1):146–157, 1993.

[29] M. Leschziner. Modelling Separation from Curved Surfaces with Anisotropy-Resolving Turbulence Closures. In *Modelling Fluid Flow*, pages 23–47. Springer, Berlin, 2004. DOI: 10.1007/978-3-662-08797-8_2.

[30] V. Kumar, B. Frohnapfel, J. Jovanovi, M. Breuer, W. Zuo, I. Hadzi, and R. Lechner. Anisotropy Invariant Reynolds Stress Model of Turbulence (AIRSM) and its Application to Attached and Separated Wall-Bounded Flows. *Flow, Turbulence and Combustion*, 83(1):81–103, July 2009.

[31] T. B. Gatski. Second-moment and scalar flux representations in engineering and geophysical flows. *Fluid Dynamics Research*, 41(1):012202, 2009.

[32] R. Smalley, S. Leonardi, R. Antonia, L. Djenidi, and P. Orlandi. Reynolds stress anisotropy of turbulent rough wall layers. *Experiments in fluids*, 33(1):31–37, 2002.

[33] S. Leonardi, P. Orlandi, L. Djenidi, and R. A. Antonia. Structure of turbulent channel flow with square bars on one wall. *International Journal of Heat and Fluid Flow*, 25(3):384–392, June 2004.

[34] C. Klipp. Turbulence Anisotropy in the Near-Surface Atmosphere and the Evaluation of Multiple Outer Length Scales. *Boundary-Layer Meteorology*, 151(1):57–77, December 2013.

[35] B. Frohnapfel, P. Lammers, J. Jovanovi, and F. Durst. Interpretation of the mechanism associated with turbulent drag reduction in terms of anisotropy invariants. *Journal of Fluid Mechanics*, 577:457–466, April 2007.

[36] P.-Å. Krogstad and L. E. Torbergsen. Invariant analysis of turbulent pipe flow. *Flow, turbulence and combustion*, 64(3):161–181, 2000.

[37] W. D. Smyth and J. N. Moum. Anisotropy of turbulence in stably stratified mixing layers. *Physics of Fluids*, 12(6):1343–1362, 2000.

[38] O. Oyewola, L. Djenidi, and R. A. Antonia. Influence of localised wall suction on the anisotropy of the Reynolds stress tensor in a turbulent boundary layer. *Experiments in Fluids*, 37(2):187–193, March 2004.

[39] R. Gómez-Elvira, A. Crespo, E. Migoya, F. Manuel, and J. Hernández. Anisotropy of turbulence in wind turbine wakes. *Journal of Wind Engineering and Industrial Aerodynamics*, 93(10):797–814, October 2005.

[40] S. C. Tedds, I. Owen, and R. J. Poole. Near-wake characteristics of a model horizontal axis tidal stream turbine. *Renewable Energy*, 63:222–235, March 2014.

[41] N. Hamilton, M. Tutkun, and R. B. Cal. Wind turbine boundary layer arrays for Cartesian and staggered configurations: Part II, low-dimensional representations via the proper orthogonal decomposition. *Wind Energy*, 18(2):297–315, February 2015.

[42] K. E. Meyer, J. M. Pedersen, and O. Özcan. A turbulent jet in crossflow analysed with proper orthogonal decomposition. *Journal of Fluid Mechanics*, 583:199–227, jul 2007.

[43] J. L. Lumley. Computational Modeling of Turbulent Flows. *Advances in Applied Mechanics*, 18:123–176, January 1979.

[44] L. P. Chamorro, R. E. A. Arndt, and F. Sotiropoulos. Reynolds number dependence of turbulence statistics in the wake of wind turbines. *Wind Energy*, 15(5):733–742, July 2012.

[45] R. B. Cal, J. Lebrón, L. Castillo, H.-S. Kang, and C. Meneveau. Experimental study of the horizontally averaged flow structure in a model wind-turbine array boundary layer. *Journal of Renewable & Sustainable Energy*, 2(1):013106, January 2010.

[46] N. Hamilton, M. Tutkun, and R. B. Cal. Anisotropic character of low-order turbulent flow descriptions through the proper orthogonal decomposition. *Physical Review Fluids*, 2(1):014601, 2017.

[47] A. Laratro, M. Arjomandi, R. Kelso, and B. Cazzolato. A discussion of wind turbine interac-

tion and stall contributions to wind farm noise. *Journal of Wind Engineering and Industrial Aerodynamics*, 127(Supplement C):1–10, April 2014.

[48] P. Moriarty and P. Migliore. Semi-empirical aeroacoustic noise prediction code for wind turbines. Technical report, National Renewable Energy Lab., Golden, CO.(US), 2003.